



# Microstructures and properties of $\text{Al}_{0.3}\text{CoCrFeNiMn}_x$ high-entropy alloys



Sze-Kwan Wong, Tao-Tsung Shun\*, Chieh-Hsiang Chang, Che-Fu Lee

Department of Materials Science and Engineering, Feng Chia University, Taichung, 407, Taiwan

## HIGHLIGHTS

- All of the alloys exhibit an FCC polycrystalline structure.
- Addition of Mn to the alloy increases the lattice parameter, hardness, yield stress, and ultimate tensile strength.
- Solid-solution strengthening and work hardening are two mechanisms behind the strengthening.
- The addition of Mn to the alloy leads to a slight deterioration of corrosion resistance.

## ARTICLE INFO

### Article history:

Received 27 March 2017

Received in revised form

11 July 2017

Accepted 31 July 2017

Available online 31 July 2017

### Keywords:

High-entropy alloy

Microstructure

Mechanical properties

Electrochemical corrosion properties

## ABSTRACT

The purpose of this study is to investigate the effects of Mn addition on the microstructure, mechanical properties, and electrochemical corrosion properties of  $\text{Al}_{0.3}\text{CoCrFeNiMn}_x$  ( $x = 0, 0.1$ , and  $0.3$ ) high-entropy alloys. All alloys are simple face-centered cubic solid solutions. After addition of Mn to the  $\text{Al}_{0.3}\text{CoCrFeNi}$  alloy, the lattice parameter and hardness increase from  $3.591 \text{ \AA}$  to  $3.611 \text{ \AA}$  and from HV141 to HV156, respectively. Meanwhile, the yield stress and ultimate tensile strength increase from 119 MPa to 158 MPa and from 295 MPa to 371 MPa, respectively. The increase in yield stress is due to solid solution strengthening, and the increase in ultimate tensile strength results from the increase in work hardening due to the reduction of stacking fault energy. Polarization curves of the alloys show that the corrosion resistance slightly decreases after additions of Mn.

© 2017 Elsevier B.V. All rights reserved.

## 1. Introduction

Developments in traditional alloy systems have focused on one or two principal elements with atomic percentages of more than 50%. High-entropy alloys, a concept proposed by Yeh et al., in 2004, comprise a new domain in alloy design [1]. These alloys typically consist of five to thirteen principal metallic elements, the concentration of which range 5–35 at.%. The alloys' properties can also be modified by adding minor elements such as interstitial C or B [2–5]. AlCoCrFeNi-based alloys with a combination of Cu, Ti, Mo, or V have been extensively studied because of the easy formation of the simple body-centered cubic (BCC) or face-centered cubic (FCC) matrix. These alloys show several attractive properties such as easy formation of nanostructure, high strength, good thermal stability, and high malleability [6–10].

Mn, one of the cheap metallic elements, is abundant in the earth's crust and is easy to utilize. It is widely used as an alloying element [11]. For instance, it can be added to steel to enhance the abilities to resist impact and wear. It can be used to substitute Ni in stainless steel in order to reduce cost. It can also increase the hardening ability of aluminum alloys. In studies on Mn-containing high-entropy alloys, adding Mn to BCC AlCrFeCoNiCu alloy resulted in the formation of a Cr-rich phase, dramatically decreasing the alloy's compressive strength and ductility [12]. However, the tensile strength of FCC CoCrFeMnNi alloy increased along with the decrease in temperature from 293 to 77 K because of deformation twinning and a decrease in stacking fault energy [13]. After annealing at 850 °C, its strength decreased because of grain coarsening [14]. This alloy also exhibited fracture resistance at both high and low temperatures [15]. The above studies indicate that the addition of Mn to an FCC high-entropy alloy may have a positive impact on its mechanical properties.

So far, very little in the literature discusses the effect of Mn content variation on the high-entropy-alloy microstructure and

\* Corresponding author.

E-mail address: [ttshun@fcu.edu.tw](mailto:ttshun@fcu.edu.tw) (T.-T. Shun).

properties. In this work, the effects of Mn additions on the microstructures and properties of  $\text{Al}_{0.3}\text{CoCrFeNiMn}_x$  ( $x = 0, 0.1$ , and  $0.3$ ) high-entropy alloys are discussed.

## 2. Material and methods

The high-entropy alloys  $\text{Al}_{0.3}\text{CoCrFeNiMn}_x$  ( $x = 0, 0.1$ , and  $0.3$ , denoting  $\text{Mn}_0$ ,  $\text{Mn}_{0.1}$ , and  $\text{Mn}_{0.3}$ , respectively) were produced through induction melting and casting in air. Elemental Al, Co, Cr, Fe, Ni, and Mn with a purity of more than 99 wt% were used as raw materials. The ingot size was approximately  $6\text{ cm} \times 8\text{ cm} \times 15\text{ cm}$ . Samples cut from the ingot were used in microstructure analysis, hardness measurement, tensile test, and electrochemical corrosion test. The microstructure was examined by scanning electron microscopy (SEM, HITACHI S-3400N) equipped with energy-dispersive spectrometry (EDS, BRUKER-XFLASH6/10). *Aqua regia* was employed as an etching solution for the SEM sample after polishing. The crystal structure was identified by X-ray diffractometer (XRD, Bruker D8 SSS) using Cu K $\alpha$  radiation at a scanning rate of  $4^\circ\text{ min}^{-1}$  and a  $2\theta$  range of  $20^\circ$ – $100^\circ$ . The hardness under a load of 300 g for duration of 15 s was measured by using a Vickers hardness tester (Future-Tech FR-300e). Five different positions were measured to calculate the average value and standard deviation. The plate-type subsizes specimens (ASTM E8) were prepared for tensile test (Chun Yen CY-6040A4 universal tensile testers) at a strain rate of  $4 \times 10^{-4}\text{ s}^{-1}$  at room temperature. The electrochemical corrosion test was performed by potentiodynamic polarization measurement using a 3.5% NaCl solution at room temperature. The test used a Biologic SP-150 potentiostat at a scan rate of  $5\text{ mV s}^{-1}$ , a segment of 1, a scan range of  $-1$  to  $1\text{ V}$ , a frequency of  $10^5$ – $10^{-2}\text{ Hz}$ , and an amplitude of  $5\text{ mV}$ .

## 3. Results and discussion

### 3.1. Crystal structure

**Fig. 1** shows the XRD patterns of the alloys  $\text{Mn}_0$ ,  $\text{Mn}_{0.1}$  and  $\text{Mn}_{0.3}$ . All alloys exhibit a simple FCC phase. Lattice parameters of alloys calculated using Bragg formula [16] are 3.591, 3.603 and 3.611 Å, respectively. The lattice parameter of the alloys increases slightly with an increase in the Mn content because the atomic radius of Mn (1.27 Å) is smaller than those of Al (1.43 Å) and Cr (1.28 Å) but slightly larger than those of Co (1.25 Å), Fe (1.26 Å), and Ni (1.24 Å). Therefore, addition of Mn to  $\text{Al}_{0.3}\text{CoCrFeNi}$  alloy induces the lattice

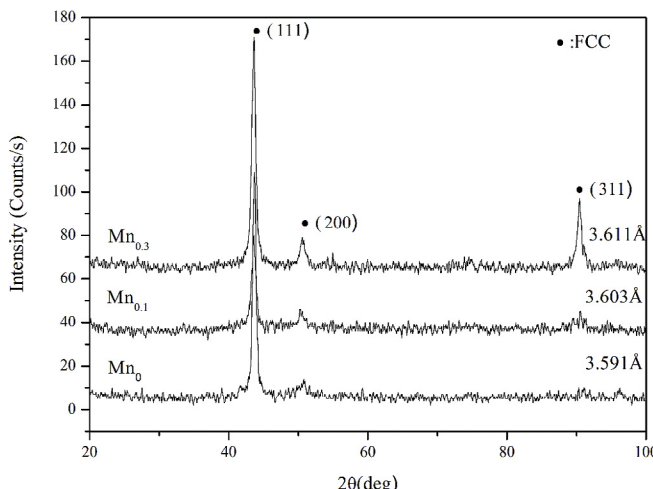


**Fig. 1.** XRD patterns of  $\text{Mn}_0$ ,  $\text{Mn}_{0.1}$ , and  $\text{Mn}_{0.3}$ .

expansion. However, this lattice expansion is not large because the amount of Mn addition is only 0.1 or 0.3 mol.

### 3.2. Microstructure

SEM images of  $\text{Mn}_0$ ,  $\text{Mn}_{0.1}$  and  $\text{Mn}_{0.3}$  are displayed in **Fig. 2**, and their chemical compositions as obtained by EDS analysis are listed in **Table 1**. All alloys exhibit a polycrystalline structure with grain size larger than 500  $\mu\text{m}$ . No secondary phase can be observed. These results confirm the XRD analyses results in **Fig. 1**, which shows that all of the alloys comprise a simple FCC solid solution. In addition, some black dots inside the grains in **Fig. 2** identified by EDS are mainly  $\text{Al}_2\text{O}_3$  inclusion, and the amount of inclusions in the three alloys is approximate (~2 vol%).

### 3.3. Hardness

**Fig. 3** shows the hardness variation of the  $\text{Al}_{0.3}\text{CoCrFeNiMn}_x$  alloys. The alloy hardness increases from HV141 to HV156 with the increase in Mn content to 6.8 at%. The strengthening of the alloy can be attributed to two effects. One is solid-solution strengthening due to lattice distortion; the increase in lattice parameter of the alloy after Mn addition (section 3.1) explains this effect. The other effect is the reduction in stacking fault energy of the alloy, which makes cross-slipping of dislocations more difficult [17]. This reduction upon the addition of the Mn may be deduced from the increase in mean electron hole number of each alloy, which is calculated by the formula  $\bar{N} = \sum_{i=1}^n miNvi$  applied in superalloys [18]. Here,  $\bar{N}$  is the average electron hole number of the alloy,  $n$  is the number of elements in the alloy,  $mi$  is the atomic percentage of a particular element, and  $Nvi$  is the electron hole number of the element (**Table 2**). The calculated mean electron hole numbers of  $\text{Mn}_0$ ,  $\text{Mn}_{0.1}$  and  $\text{Mn}_{0.3}$  are 2.44, 2.47, and 2.52, respectively. Thus, the mean electron hole number increases upon addition of Mn.

### 3.4. Tensile properties

**Fig. 4** shows the engineering stress-strain curves obtained from tensile tests for  $\text{Mn}_0$ ,  $\text{Mn}_{0.1}$  and  $\text{Mn}_{0.3}$ . **Table 3** summarizes data for the yield stress ( $\sigma_y$ ), ultimate tensile strength ( $\sigma_{UTS}$ ), elongation, and extent of work hardening ( $\Delta\sigma = \sigma_{UTS} - \sigma_y$ ). Evidently,  $\sigma_y$ ,  $\sigma_{UTS}$ , and  $\Delta\sigma$  respectively increase from 119 to 158 MPa, from 295 to 371 MPa, and from 176 to 213 MPa with the increase in Mn content, while the elongation declines from 59% to 46%. The increase in  $\sigma_y$  is due to solid-solution strengthening, and the increase in  $\sigma_{UTS}$  results from the increase in work hardening due to the reduction in stacking fault energy. Engineering stress-strain curves of all of the alloys (**Fig. 4**) have a yield point that is related to the homogeneously spherical nanoprecipitates with the L12 ordered structure reported in our previous study [19]. These nanoprecipitates act as coherent GP zones, and the dislocation cutting through the particle results in a drop in the yield.

**Fig. 5** shows SEM images of the polished surface of  $\text{Mn}_0$ ,  $\text{Mn}_{0.1}$ , and  $\text{Mn}_{0.3}$  under tension. Clearly, the deformation marks of the three alloys differ: that of the  $\text{Mn}_0$  has a wavy glide, and that of  $\text{Mn}_{0.3}$  has a planar glide, and that of  $\text{Mn}_{0.1}$  contains both types. The wavy glide created by a material with high stacking fault energy and narrowly separated partial dislocations facilitates cross-slipping of dislocations and results in lower work hardening during deformation. Conversely, the planar glide is a material with low stacking fault energy and widely separated partial dislocations, indicating more difficult for cross-slipping of dislocations and higher work hardening [20]. The characteristics of the deformation mark on each alloy's surface thus confirm the effects of reduction in

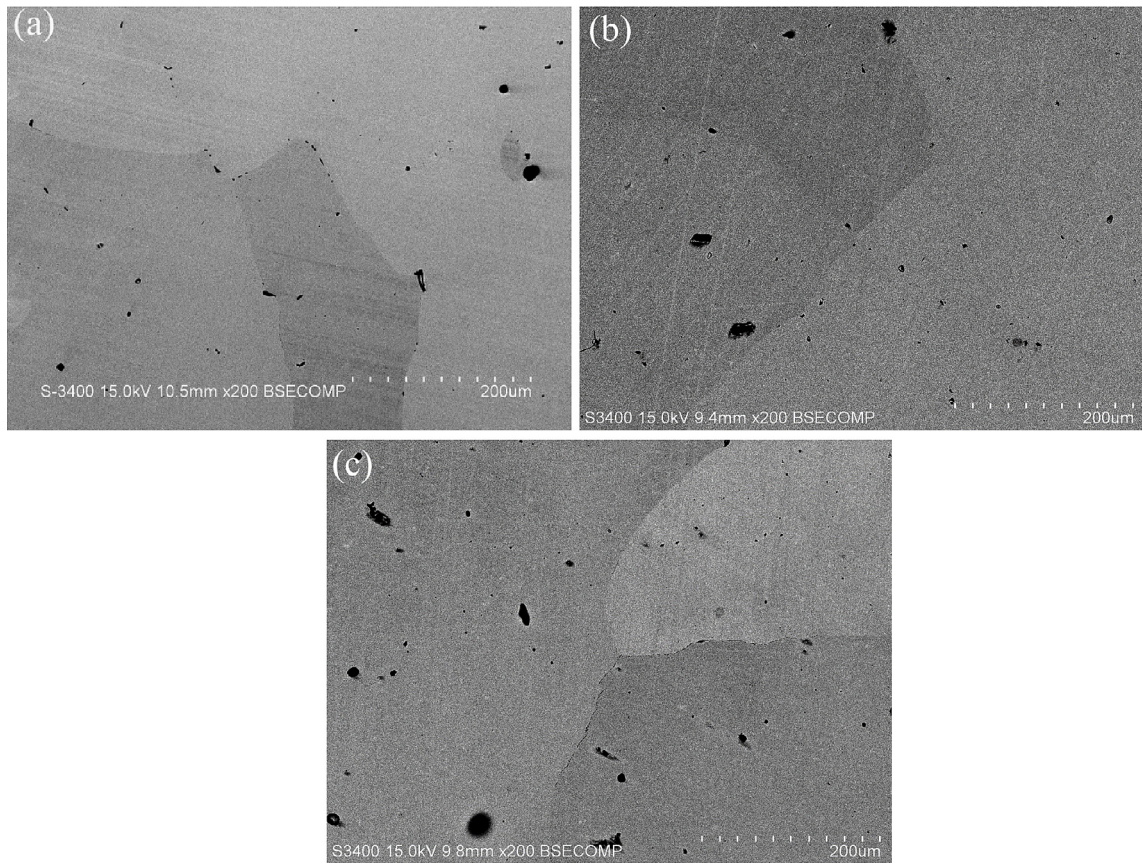


**Fig. 2.** SEM images of the alloys (a) Mn<sub>0</sub>, (b) Mn<sub>0.1</sub>, and (c) Mn<sub>0.3</sub>.

**Table 1**  
Chemical compositions (at%) of Al<sub>0.3</sub>CoCrFeNiMn<sub>x</sub> alloys.

Alloy	Al	Co	Cr	Fe	Ni	Mn
Al <sub>0.3</sub> CoCrFeNi	6.9	23.3	23.4	23.3	23.1	N/A
Al <sub>0.3</sub> CoCrFeNiMn <sub>0.1</sub>	6.8	22.5	23.0	22.9	22.4	2.4
Al <sub>0.3</sub> CoCrFeNiMn <sub>0.3</sub>	6.2	21.2	21.7	21.9	22.2	6.8

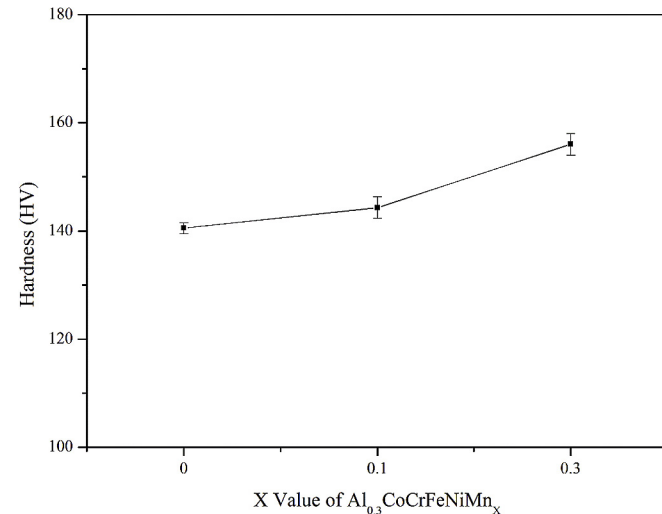


**Fig. 3.** Variation of hardness of Al<sub>0.3</sub>CoCrFeNiMn<sub>x</sub> alloys.

**Table 2**  
Electron hole number of individual element in alloy [17,18].

	Al	Co	Cr	Fe	Ni	Mn
Electron hole number	2.66	1.71	4.66	2.66	0.66	3.66

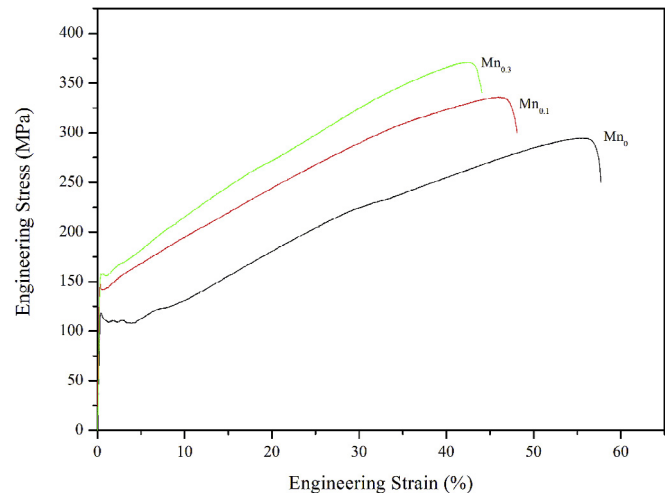


**Fig. 4.** Tensile stress–strain curves of Mn<sub>0</sub>, Mn<sub>0.1</sub>, and Mn<sub>0.3</sub>.

**Table 3**

Yield stress ( $\sigma_y$ ), ultimate tensile strength ( $\sigma_{UTS}$ ), elongation, and extent of work hardening ( $\Delta\sigma = \sigma_{UTS} - \sigma_y$ ) of  $Mn_0$ ,  $Mn_{0.1}$  and  $Mn_{0.3}$ .

Alloy	$\sigma_y$ (MPa)	$\sigma_{UTS}$ (MPa)	Elongation (%)	$\Delta\sigma$ (MPa)
$Mn_0$	119	295	59	119
$Mn_{0.1}$	149	336	49	149
$Mn_{0.3}$	158	371	46	158

stacking fault energy and the increase in strength upon addition of Mn to the alloys.

### 3.5. Electrochemical corrosion properties

Polarization curves of the alloys and of SUS304 stainless steel are showed in Fig. 6, and their electrochemical parameters are listed in Table 4. The corrosion potentials ( $E_{corr}$ ) of  $Mn_0$ ,  $Mn_{0.1}$ ,  $Mn_{0.3}$  and SUS304 are  $-0.169$ ,  $-0.172$ ,  $-0.189$ , and  $-0.215$  V, respectively. This result indicates that the three high-entropy alloys have corrosion resistance better than that of SUS304. This result is due to the higher content of the anticorrosive elements Cr and Ni in the alloys as compared with that of SUS304. Fig. 6 also shows the polarization curves of  $Mn_0$ ,  $Mn_{0.1}$  and  $Mn_{0.3}$  mostly overlap, suggesting that the three alloys are almost identical in terms of corrosion resistance. The value of  $E_{corr}$  (Table 4) indicates that the addition of Mn to the alloy leads to slight deterioration of the corrosion resistance. This deterioration is due to the increase in Mn content and the concomitant reduction of the Cr and Ni content.

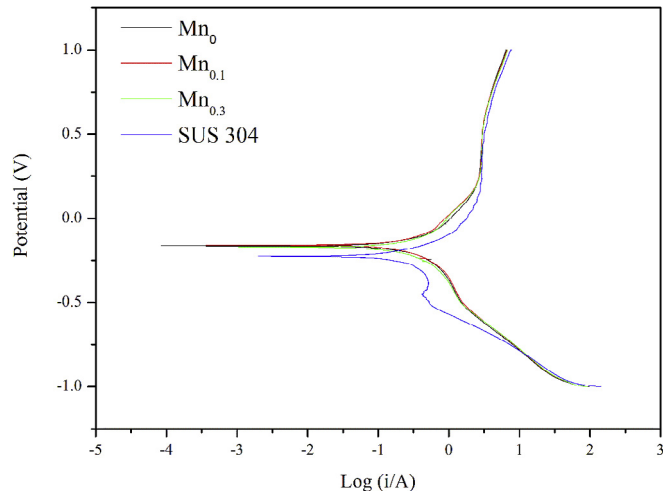


Fig. 6. Polarization curves of  $Mn_0$ ,  $Mn_{0.1}$ , and  $Mn_{0.3}$  alloys and of SUS304 stainless steel.

**Table 4**

Electrochemical parameters of  $Mn_0$ ,  $Mn_{0.1}$ ,  $Mn_{0.3}$  and SUS304.

Alloy	$E_{corr}$ (V)	$I_{corr}$ (mA/cm <sup>2</sup> )	$E_p$ (V)
$Mn_0$	$-0.169$	0.334	0.592
$Mn_{0.1}$	$-0.172$	0.325	0.579
$Mn_{0.3}$	$-0.189$	0.331	0.554
SUS304	$-0.215$	0.324	0.613

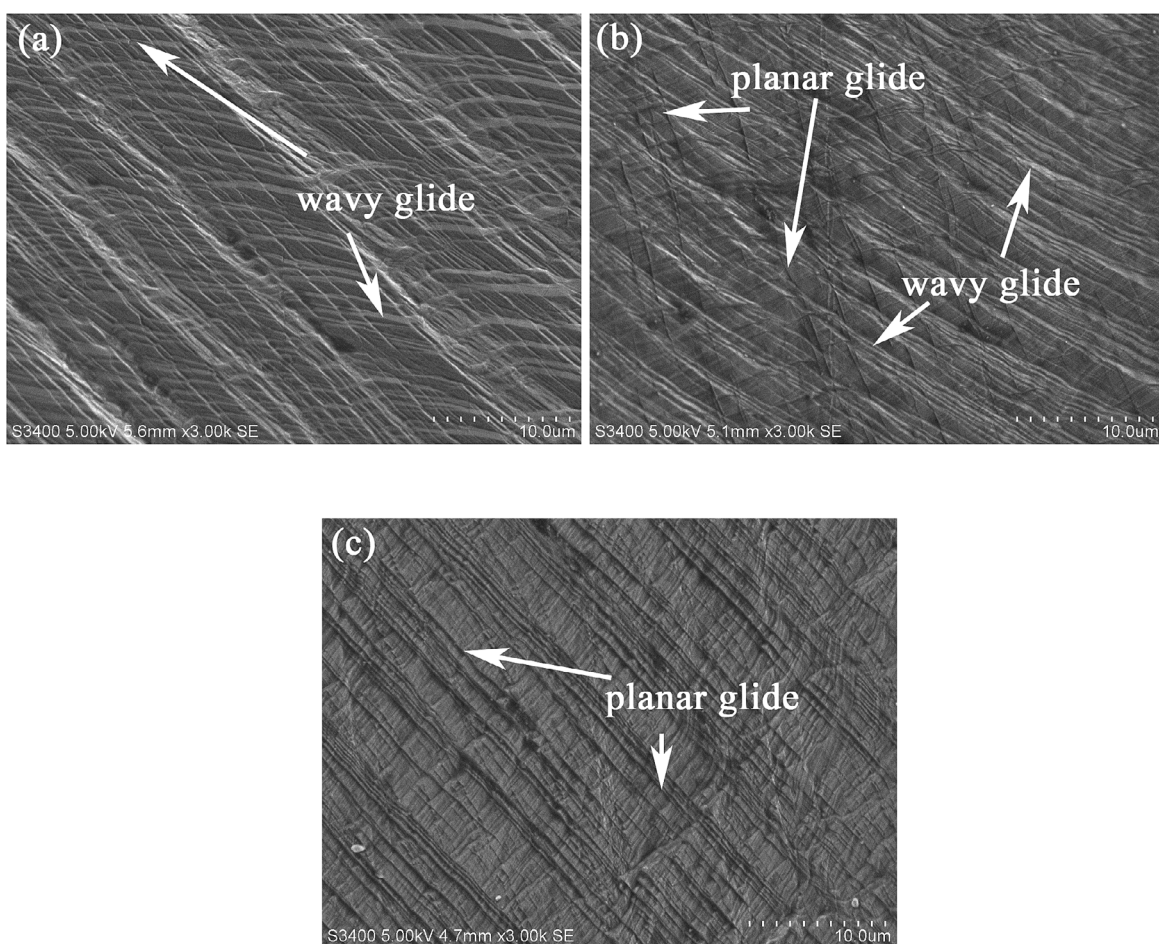
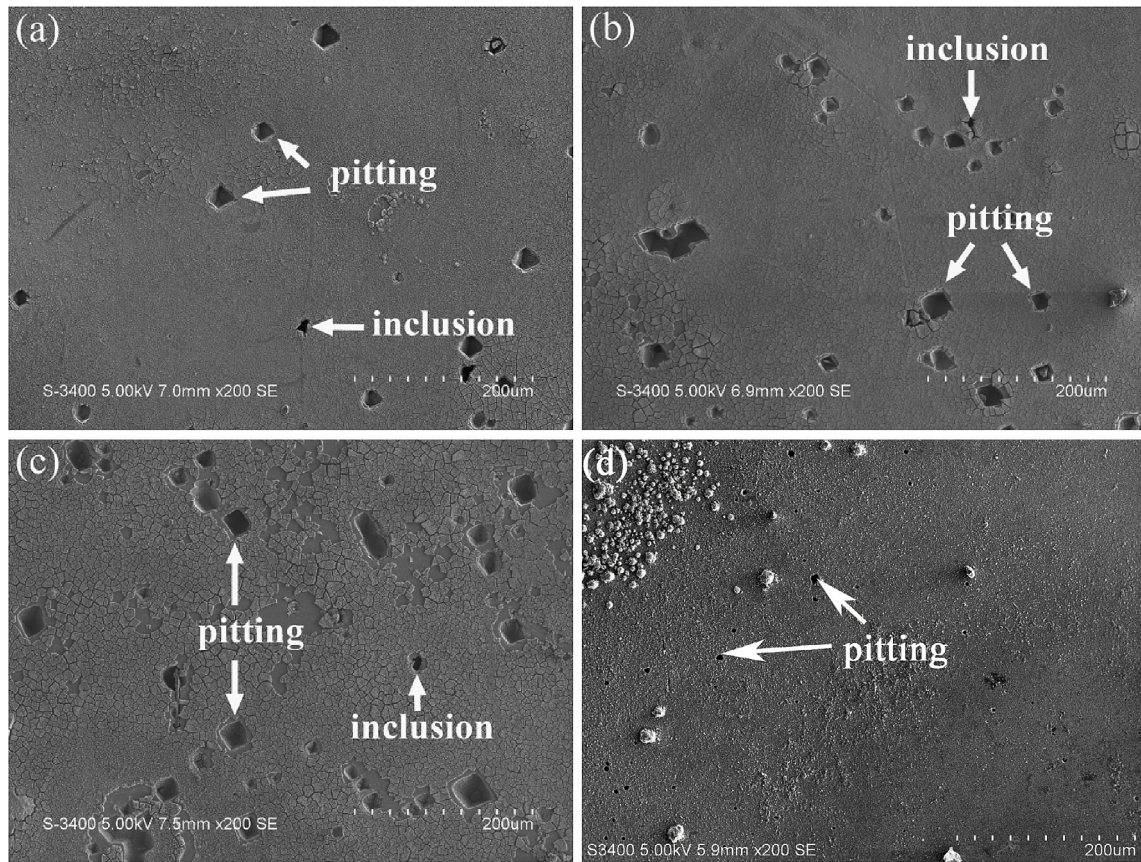


Fig. 5. SEM images of the polished surfaces of the alloys under tension: (a)  $Mn_0$ , (b)  $Mn_{0.1}$ , and (c)  $Mn_{0.3}$ .



**Fig. 7.** SEM images of the surface after electrochemical corrosion of (a) Mn<sub>0</sub>, (b) Mn<sub>0.1</sub>, (c) Mn<sub>0.3</sub>, and (d) SUS304.

The pitting potentials ( $E_p$ ) of Mn<sub>0</sub>, Mn<sub>0.1</sub>, Mn<sub>0.3</sub>, and SUS304 are 0.592, 0.579, 0.554, and 0.613 V, respectively. The pitting resistances of the three alloys are thus lower than that of SUS304. Fig. 7 shows SEM images of the surface after electrochemical corrosion of Mn<sub>0</sub>, Mn<sub>0.1</sub>, Mn<sub>0.3</sub>, and SUS304. The appearances of most pitting pores and inclusions in Mn<sub>0</sub> to Mn<sub>0.3</sub> alloys after testing are dark-gray square shape and black irregular shape, respectively. We suggest that these inclusions in alloys will somewhat deteriorate the pitting resistance. However, this effect can be ignored in evaluation of pitting resistance among the present three high-entropy alloys due to their approximate inclusion content. Comparison of the number of pitting holes on each alloy agrees with the evaluation of pitting resistance from the  $E_p$  value. The pitting resistance equivalent number (PRE<sub>N</sub>) of stainless steel is expressed as  $\text{PRE}_N = \text{Cr} + 1.1\text{Mo} + 40.3\text{N} - 1.3\text{Mn}$  [21]. This equation is always used to predict the pitting resistance of the alloy in a Cl<sup>-</sup>-containing solution. Because Mn reduces the PRE<sub>N</sub>, addition of Mn to the alloy has an adverse effect on the pitting resistance. Calculated PRE<sub>N</sub> values of Mn<sub>0</sub>, Mn<sub>0.1</sub>, Mn<sub>0.3</sub>, and SUS304 are 12.09, 10.20, 6.65, and 18.06, respectively, which are in accordance with the experimental results.

#### 4. Conclusions

In this study, the effect of Mn addition on the microstructures, mechanical properties, and electrochemical corrosion properties of Al<sub>0.3</sub>CoCrFeNiMn<sub>x</sub> ( $x = 0, 0.1, 0.3$ ) high-entropy alloys were investigated. The results show that all of the alloys exhibit an FCC polycrystalline structure. After the addition of Mn to Al<sub>0.3</sub>CoCrFeNi alloy, the lattice parameter, hardness, yield stress, and ultimate

tensile strength respectively increase from 3.591 Å to 3.611 Å, from HV141 to HV156, from 119 MPa to 158 MPa, and from 295 MPa to 371 MPa. Solid-solution strengthening due to lattice distortion and work hardening due to reduction of stacking fault energy are two mechanisms behind the strengthening. The addition of Mn to the Al<sub>0.3</sub>CoCrFeNi alloy leads to a slight deterioration of corrosion resistance.

#### Acknowledgement

The authors would express gratitude for the financial support by the Ministry of Science and Technology of Taiwan under Grant No. MOST 104-2221-E-035-013. The authors also appreciate the Precision Instrument Support Center of Feng Chia University in providing the fabrication and measurement facilities.

#### References

- [1] J.W. Yeh, S.K. Chen, J.Y. Gan, T.S. Chin, T.T. Shun, C.H. Tsau, S.Y. Chang, Nanostructured high-entropy alloys with multiple principal elements: novel alloy design concepts and outcomes, *Adv. Eng. Mater.* 6 (5) (2004) 299–303.
- [2] Z. Wang, I. Baker, Z. Cai, S. Chen, J.D. Poplawsky, W. Guo, The effect of interstitial carbon on the mechanical properties and dislocation substructure evolution in Fe<sub>40.4</sub>Ni<sub>11.3</sub>Mn<sub>34.8</sub>Al<sub>7.5</sub>Cr<sub>6</sub> high entropy alloys, *Acta. Mater.* 120 (2016) 228–239.
- [3] Z. Wu, M. Parish, H. Bei, Nano twin mediated plasticity in carbon containing FeNiCoCrMn high entropy alloys, *J. Alloy. Compd.* 647 (2015) 815–822.
- [4] Z. Li, C.C. Tasan, H. Springer, B. Gault, D. Raabe, Interstitial atoms enable joint twinning and transformation induced plasticity in strong and ductile high-entropy alloys, *Sci. Rep.* 7 (40704) (2017) 1–7.
- [5] Z. Wang, I. Baker, Interstitial strengthening of a fcc FeNiMnAlCr high entropy alloy, *Mater. Lett.* 180 (2016) 153–156.
- [6] Y. Dong, K. Zhou, Y. Lu, X. Gao, T. Wang, T. Li, Effect of vanadium addition on the microstructure and properties of AlCoCrFeNi high entropy alloy, *Mater.*

- Des. 57 (2014) 67–72.
- [7] Y.J. Zhou, Y. Zhang, F.J. Wang, Y.L. Wang, G.L. Chen, Effect of Cu addition on the microstructure and mechanical properties of AlCoCrFeNiTi<sub>0.5</sub> solid-solution alloy, *J. Alloy. Compd.* 466 (2008) 201–204.
- [8] J.M. Zhu, H.M. Fu, H.F. Zhang, A.M. Wang, H. Lia, Z.Q. Hua, Microstructures and compressive properties of multicomponent AlCoCrFeNiMo<sub>x</sub> alloys, *Mater. Sci. Eng. A* 527 (2010) 6975–6979.
- [9] C.F. Lee, T.T. Shun, Effect of Fe content on microstructure and mechanical properties of Al<sub>0.5</sub>CoCrFe<sub>x</sub>NiTi<sub>0.5</sub> high entropy alloys, *Mater. Charact.* 114 (2016) 179–184.
- [10] I.S. Wani, T. Bhattacharjee, S. Sheikh, P.P. Bhattacharjee, S. Guo, N. Tsuji, Tailoring nanostructures and mechanical properties of AlCoCrFeNi<sub>2.1</sub> eutectic high entropy alloy using thermos mechanical processing, *Mat. Sci. Eng. A* 675 (2016) 99–109.
- [11] G.E. Totten, L. Xie, K. Funatani, *Handbook of Mechanical Alloy Design*, Marcel Dekker, Inc., New York, 2004.
- [12] B.S. Li, Y.P. Wang, M.X. Ren, C. Yang, H.Z. Fu, Effects of Mn, Ti and V on the microstructure and properties of AlCrFeCoNiCu high entropy alloy, *Mat. Sci. Eng. A* 498 (2008) 482–486.
- [13] F. Otto, A. Dlouhý, Ch. Somsen, H. Bei, G. Eggeler, E.P. George, The influences of temperature and microstructure on the tensile properties of a CoCrFeMnNi high-entropy alloy, *Acta. Mater.* 61 (2013) 5743–5755.
- [14] W.H. Liu, Y. Wu, J.Y. He, T.G. Nieh, Z.P. Lu, Grain growth and the Hall-Petch relationship in a high-entropy FeCrNiCoMn alloy, *Scr. Mater.* 68 (2013) 526–529.
- [15] B. Gludovatz, et al., A fracture-resistant high-entropy alloy for cryogenic applications, *Sci.* 345 (2014) 1153–1158.
- [16] B.D. Cullity, S.R. Stock, *Elements of X-ray Diffraction*, third ed., Prentice-Hall, Inc., New Jersey, 2001.
- [17] W.F. Smith, *Structure and Properties of Engineering Alloys*, second ed., McGraw-Hill, Inc., 1993.
- [18] C.T. Sims, N.S. Stoloff, W.C. Hagel, *Superalloys II*, John Wiley & Sons, Inc., 1987.
- [19] T.T. Shun, Y.C. Du, Microstructure and tensile behaviors of FCC Al<sub>0.3</sub>CoCrFeNi high entropy alloy, *J. Alloy. Compd.* 479 (2009) 157–160.
- [20] R.W. Hertzberg, *Deformation and Fracture Mechanics of Engineering Materials*, second ed., John Wiley & Sons, Inc., 1983.
- [21] M.O. Speidel, R.M. Pedrazzoli, High nitrogen stainless steels in chloride solutions, *Mater. Perform.* 31 (9) (1992) 59–61.